Research Article | Vol. 13, No. 11 / 1 Nov 2022 / Biomedical Optics Express 5574
Biomedical Optics EXPRESS

3D super-resolution live-cell imaging with radial symmetry and Fourier light-field microscopy

KEYI HAN,[1] XUANWEN HUA,[1] VISHWA VASANI,[2] GE-AH R. KIM,[3] WENHAO LIU,[1] SHUICHI TAKAYAMA,[1,4] AND SHU JIA[1,4,*]

[1]*Wallace H. Coulter Department of Biomedical Engineering, Georgia Institute of Technology and Emory University, Atlanta, GA, 30332, USA*
[2]*George W. Woodruff School of Mechanical Engineering, Georgia Institute of Technology, Atlanta, GA, 30332, USA*
[3]*School of Materials Science and Engineering, Georgia Institute of Technology, Atlanta, GA, 30332, USA*
[4]*Parker H. Petit Institute for Bioengineering and Bioscience, Georgia Institute of Technology, Atlanta, GA, 30332, USA*
[*]*shu.jia@gatech.edu*

Abstract: Live-cell imaging reveals the phenotypes and mechanisms of cellular function and their dysfunction that underscore cell physiology, development, and pathology. Here, we report a 3D super-resolution live-cell microscopy method by integrating radiality analysis and Fourier light-field microscopy (*rad*-FLFM). We demonstrated the method using various live-cell specimens, including actins in Hela cells, microtubules in mammary organoid cells, and peroxisomes in COS-7 cells. Compared with conventional wide-field microscopy, *rad*-FLFM realizes scanning-free, volumetric 3D live-cell imaging with sub-diffraction-limited resolution of ~150 nm (*x*-*y*) and 300 nm (*z*), milliseconds volume acquisition time, six-fold extended depth of focus of ~6 μm, and low photodamage. The method provides a promising avenue to explore spatiotemporal-challenging subcellular processes in a wide range of cell biological research.

1. Introduction

Living cells orchestrate intracellular molecules, organelles, and microenvironments to regulate biological processes. A detailed picture of these diverse anatomical and functional characteristics enables critical insights into cell phenotypes, functions, and mechanisms. Indeed, over the past decades, fluorescence microscopy and associated methods have emerged as one of the most vital and informative driving forces for cell biological research, enabling the systematic, quantitative investigation of cellular systems [1–4].

To study living samples, in essence, the extent of biological phenomena achievable is fundamentally determined by the maximal photon budget extracted from the fluorescent signal while maintaining the sample health [5]. Under this context, conventional live-cell microscopy suffers limitations and trade-offs between four major practical considerations: spatial resolution, imaging speed, image quality (or signal-to-noise ratio – SNR), and sample health [5–7]. Unfortunately, they cannot be optimized simultaneously, which poses the main challenge for fluorescence microscopy. For example, for cell imaging, gaining a faster imaging speed at a higher frame rate, or longer observation at a reduced exposure time or illumination level, may sacrifice the SNR. As a result, these constraints inevitably compromise the imaging capability and accurate identification of fluorescent signals, especially challenging the live and quantitative interrogation of biological systems.

In response, various strategies have been developed to address every particular technical aspect mentioned above for live-cell microscopy. *First*, for instance, the development of super-resolution fluorescence imaging techniques (e.g., STORM, (f)PALM, STED, SIM) in the past two decades has overcome the physical barrier of optical microscopy and achieved fluorescence imaging with

#471967 https://doi.org/10.1364/BOE.471967
Journal © 2022 Received 2 Aug 2022; revised 23 Sep 2022; accepted 26 Sep 2022; published 3 Oct 2022

Biomedical Optics EXPRESS

a sub-diffraction-limited resolution [8–10]. In addition, analytical approaches (e.g., SOFI, SRRF) have been reported to reveal the super-resolution details of conventional images through the analysis of the intrinsic fluorescent data property [11–17]. However, the greater spatial resolution and volumetric information are typically obtained at the expense of extended acquisitions for reconstruction or fluctuation analysis, leading to compromised temporal resolution for live imaging. *Second*, on the other hand, light-field microscopy (LFM) techniques [18–21], especially the recent advance in Fourier light-field microscopy [22–25] (FLFM, or extended LFM – XLFM), realize volumetric snapshot and scanning-free recording of various biological systems at cellular to subcellular, milliseconds spatiotemporal resolution and minimum photodamage per volumetric rendering [26–29]. However, high-resolution live-cell imaging with FLFM remains diffraction-limited [30], and the recent super-resolution extension (termed SMLFM [31]) has only been demonstrated with fixed cells and a low temporal resolution owing to its dependence on 3D single-molecule detection. *Lastly*, recent years have witnessed the development of denoising models (e.g., NCS, ACsN) to enhance the SNR and thus the content and quality of fluorescence microscopy images to facilitate fast, low-light, and quantitative imaging [32–35]. In general, despite significant improvements stemming from the abovementioned efforts, a method that effectively integrates the advances of all these technical aspects for live-cell imaging remains unexplored yet highly desired.

Here, we present a 3D live-cell super-resolution imaging method based on radial symmetry analysis and Fourier light-field microscopy (*rad*-FLFM). In particular, *rad*-FLFM combines image denoising, radiality analysis, and light-field imaging to realize live-cell microscopy with 3D super-resolution, volumetric scanning-free acquisition, high specificity and sensitivity, low photodamage, and platform accessibility. The advances of *rad*-FLFM are achieved through three practical considerations: (1) *rad*-FLFM exploits effective image denoising to mitigate the temporal measurement, which is otherwise time-consuming but demanded for radiality analysis, allowing to enhance an elemental light-field image using a single camera frame; (2) *rad*-FLFM achieves super-resolution in all three dimensions across an extended imaging depth based on the computational synthesis of the radiality map of the elemental light-field image; (3) *rad*-FLFM retains the advantage of light-field imaging for the ultrafast, scanning-free and volumetric acquisition of biological specimens. We demonstrated the system using various live subcellular biological specimens, including actins in Hela cells, microtubules in mammary organoid cells, and peroxisome in COS-7 cells. Compared to wide-field microscopy, the results exhibit a two-fold improvement in 3D resolution over the diffraction limit, a six-fold extension of the imaging depth, and a temporal resolution of up to milliseconds per volume. We anticipate *rad*-FLFM to promise new developments of 3D super-resolution microscopy and a broad range of applications for live-cell imaging and cell biological discoveries.

2. Methods

2.1. Experimental setup

The *rad*-FLFM system was constructed based on high-resolution Fourier light-field microscopy [30]. In brief, the system utilizes an epi-fluorescence microscope (Nikon Eclipse Ti2-U), which is equipped with 488-nm and 647-nm laser lines (MPB Communication) and a 100×, 1.45NA objective lens (Nikon CFI Plan Apochromat Lambda 100× Oil) (**Fig. 1(a)**). The native image plane (NIP) is Fourier-transformed using a doublet lens ($f_{\mathrm{FL}} = 275$ mm, Thorlabs), and a customized hexagonal microlens array (MLA, pitch $d = 3.25$ mm, f-number $= 36$, $f_{\mathrm{ML}} = 117$ mm, RPC Photonics) is placed at the back focal plane. The three microlenses that partition the entire pupil form elemental light-field images onto an sCMOS camera (Hamamatsu ORCA-Flash 4.0, pixel size $P_{\mathrm{CAM}} = 6.5$ μm).

Biomedical Optics EXPRESS

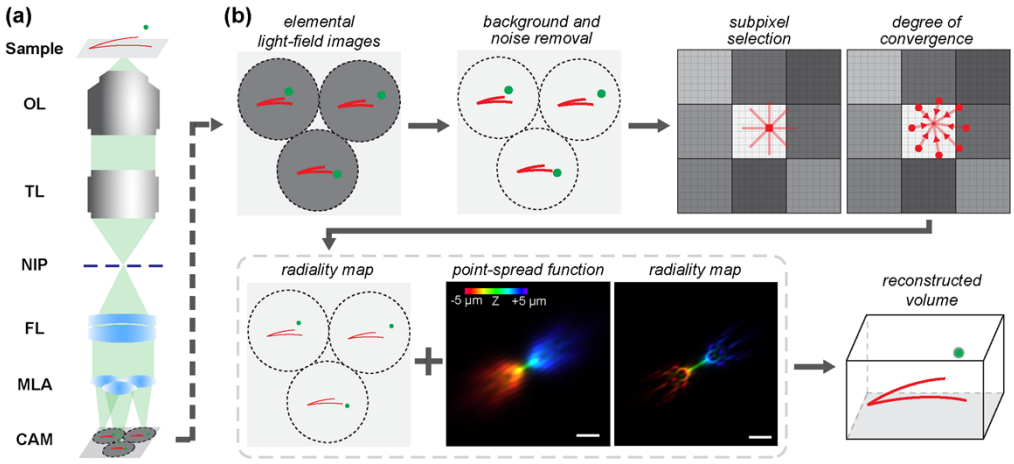

Fig. 1. Design and framework of *rad*-FLFM. (a) Emitted fluorescence from the sample is collected by an objective lens (OL) and tube lens (TL). The wide-field image is formed at the native image plane (NIP) and transformed through a doublet Fourier lens (FL). A microlens array (MLA) is placed at the conjugate pupil plane and forms three elemental light-field images on a camera (CAM). **(b)** The elemental light-field images from the camera are sequentially processed with background and noise removal, radiality analysis, and volumetric reconstruction. The reconstruction utilizes the radiality maps of both the elemental light-field images and the hybrid point-spread function (PSF) of the FLFM system. Scale bars: 2 µm.

2.2. Framework of rad-FLFM

The *rad*-FLFM method contains three key components (**Fig. 1(b)**): (2.2.1) background and noise removal, (2.2.2) radiality analysis, and (2.2.3) volumetric reconstruction.

2.2.1. Background and noise removal

First, the noise influence on the raw light-field elemental images was mitigated using our lab-written algorithm for automatic correction of sCMOS noise (ACsN) [33], followed by a rolling-ball algorithm to alleviate the remaining background patterns [36]. Notably, this initial procedure of image restoration is a crucial component of the *rad*-FLFM framework. As known, live-cell imaging necessitates a short exposure to sustain the sample health and fast imaging to capture dynamic processes, thus leading to raw fluorescent image data with low SNRs. On the other hand, the deconvolution-based reconstruction process of light-field imaging is highly sensitive and may cause miscalculated 3D object or computational artifacts due to a low image SNR. Therefore, this procedure is essential for general 3D volumetric light-field reconstruction. Furthermore, another remarkable advantage of the denoising step is that it can remove the non-fluorophore-associated peaks from raw images that typically deteriorates the radiality measurement [33]. As a result, this procedure permits viable subsequent radiality analysis using a single camera frame without any temporal averaging (e.g., SRRF may require up to 100 frames to render a super-resolution image) [14], i.e., avoiding compromising the temporal resolution of the light-field acquisition (Appendix 1 and **Table 1**).

2.2.2. Radiality analysis

Next, we utilized the radiality distribution to enhance the elemental light-field images. In practice, the radiality map is generated based on the assumption that an image, as a convolution result of the object with the point-spread function (PSF) of the imaging system, displays a high degree of local symmetry than the background. The gradient map of the image should exhibit radial

Biomedical Optics EXPRESS

symmetry, and the convergence of local gradients indicates the location and intensity of the corresponding fluorophores [12,14].

For *rad*-FLFM, the elemental light-field image (pixel size = 145 nm at the camera plane) is initially convolved with differential kernel pairs in both lateral directions to generate the gradient map, followed by Catmull-Roll spline interpolation to form the continuous space at the subpixel level to avoid any aliasing. For each location, a ring of $N = 8$ neighboring interpolated subpixels (subpixel size = 18.125 nm) that are equally distributed with a radius of $l = 0.5$ pixels is selected (**Fig. 1(b)**, subpixel selection), and the degree of convergence for one subpixel is calculated using the gradient line, the perpendicular distance to the line, and the distance from the subpixel to the center (**Fig. 1(b)**, degree of convergence). The radiality at the center location is thus defined as the average of all the degrees of convergence. For the ring of subpixels close to the center of local convergence (i.e., an actual fluorescent peak), the radiality of the subpixel at the center of the ring exhibits a higher value. The final image is rendered to 2× magnification of the original elemental light-field image (final pixel size = 72.5 nm at the camera plane) for the ease of 3D reconstruction. The radiality analysis was performed using the SRRF-plugin on ImageJ [12] with custom settings (i.e., Gradient Smoothing, Intensity Weighting, and Minimize SRRF patterning) and the input of a single ACsN- and background-processed 2D elemental light-field image.

2.2.3. 3D super-resolution volumetric reconstruction

Lastly, unlike conventional FLFM processing of intensity images [23,25], the reconstruction of *rad*-FLFM utilizes the corresponding radiality maps of both the 2D elemental light-field image and the 3D PSF (**Fig. 1(b)**, dashed boxed panel). In addition, for the generation of the 3D PSF, we adopted our strategy of hybrid PSFs for better reconstruction quality [28,30]. The volumetric synthesis of *rad*-FLFM is conducted as an inverse problem using the Richardson-Lucy deconvolution [37–39], iteratively projecting between the 3D object space and the two radiality maps. In this work, the pixel size at the NIP is 65 nm. To match the 2× magnified resolution of the elemental light-field image after the radiality analysis, the sampling intervals for the reconstruction of the object space are given as $\Delta_{xy} = 32.5$ nm, and $\Delta_z = 100$ nm after interpolation. Here, using regular CPU processing (Intel Core i9-10900X, 256 GB RAM), a volumetric iteration can be completed within 40 s, obtaining the reconstruction of an entire volume in 120-200 s using 3-5 iterations depending on the cell structure. For comparison, the conventional FLFM images were reconstructed with 50 iterations for the best quality. With a lower sampling rate, each iteration costs about 11 s using the same CPU processing.

Notably, *rad*-FLFM presents a novel concept and pipeline for 3D super-resolution rendering, i.e., the analysis of radial symmetry enhances the 2D elemental light-field image that actually contains both the spatial and angular information, which by taking advantage of image denoising and light-field synthesis, offers improved spatial resolution in all three dimensions without compromising the volumetric acquisition speed and photodamage.

2.3. Materials and sample preparation

Actin imaging was performed with HeLa cells (Sigma-Aldrich, #93021013). The cells were cultured in Dulbecco's modified Eagle medium (DMEM, Corning, #10-013-CV) with 10% fetal bovine serum (FBS, Corning, #35-011-CV) and 1% Penicillin-Streptomycin (Pen-Strep, ThermoFisher, #15140122) at 37 °C and in a 5% CO_2 atmosphere. On the day of imaging, the cells were stained in 3 mL modified DMEM and 3 µL of CellMask Green Actin Tracking Stains (ThermoFisher, #A57243), incubating for 45 minutes. Then the culture medium was removed, and the cells were washed twice with clear HBSS (Corning, #21-021-CV). Finally, 2 mL of live cell imaging buffer (ThermoFisher, #A14271DJ) was added to the sample dish for imaging.

Mammary organoid is prepared using hanging drop method [40,41]. For the 2D culture, MCF10A cells were purchased from the American Type Culture Collection (ATCC) and were

Biomedical Optics EXPRESS

grown in DMEM/F12 (Gibco, #11330-032) supplemented with 5% horse serum (Gibco, #16050-122), 20 ng/mL HB-EGF (Peprotech, #100-47), 0.5 µg/mL hydrocortisone (Sigma-Aldrich, #H0888), 100 ng/mL Cholera toxin (Sigma-Aldrich, #C8052), 10 µg/mL insulin (Sigma-Aldrich, #I1882) and 1% Penicillin-Streptomycin (Gibco, #15140-163). 2D cultures were maintained at 37 °C and 5% CO_2 in T75 culture flasks. Cells were passaged when they reached 70–80% confluence. To acquire 3D MCF10A mammary organoids, a 384 well custom-made hanging drop plate was used [42], which was soaked overnight in 0.1% F108 pluronic solution (Sigma, 542342) in DI water, rinsed with DI water, air dried, and UV sterilized for 20 mins on each side with a UVP Crosslinker (Analytik Jena). To maintain humidity for the droplets, the hanging drop plate was placed between the bottom and the lid of a 96 well round bottom plate, each well filled with 150 µL of DI water supplemented with 1% pen-strep. To further prevent evaporation near the plate edges, the hanging drop plate troughs were filled with DI water supplemented with 1% pen-strep, and sterile gauze pad. 3000 MCF10A cells were seeded in every alternate well of the hanging drop plate with 25 µL of the seeding solution, which in-turn consisted of previously described 2D cell culture medium, warmed, and further supplemented with (warm) 10% FBS (GeminiBio, #900-108), (warm) 0.24% Methylcellulose (Sigma-Aldrich, #94378-100G) and (cold) 1.5% Matrigel (Corning, #356-231). On day 3 of organoid culture, seeding supplements were washed out by exchanging the media 3 times with a CyBio FeliX liquid handling machine (Analytik Jena), and after that the media was exchanged 2 times every 2–3 days.

Organoids were collected on day 12 and were transferred into a 30 mm culture dish (Falcon, #353001) containing grown medium. After 9 days of incubation at 37 °C and 5% CO_2, the MCF10A cells sit and spread on the bottom of the dish. At the day of imaging, 30 µL of Tubulin Tracker Deep Red (ThermoFisher, #T34077) was added. After 45 min incubation at 37 °C and 5% CO_2, wash media was carefully removed without disturbing the organoids and was replaced by 2 mL of live cell imaging buffer for imaging.

Peroxisome imaging was performed with COS-7 cells (Sigma-Aldrich, #87021302). Similar to HeLa cell culturing, COS-7 cells were cultured in DMEM with 10% FBS, and 1% Pen-Strep at 37 °C and in a 5% CO_2 atmosphere. For single-color live-cell imaging, the cells were grown in a pre-warmed (37 °C) mixed solution containing 3 mL modified DMEM and 15 µL CellLight Peroxisome-GFP (ThermoFisher, # C10604). The GFP was expressed on the peroxisomes in the cells after overnight cell growth. Then the culture medium was removed, and the cells were washed twice with clear HBSS. Lastly, 2 mL FluoroBrite DMEM (ThermoFisher, #A1896701) was added into the sample for imaging.

3. Results

3.1. Imaging actins in live HeLa cells

To validate *rad*-FLFM, we first performed light-field imaging of actins in live HeLa cells using the 488-nm laser (**Fig. 2**). Conventionally, as seen, the FLFM system acquired the distinct perspective views of the sample in three elemental images, allowing us to reconstruct the cell using a single camera frame at a volume acquisition time of 0.2 s (**Fig. 2(a,b)**). Here, using *rad*-FLFM, the spatial details of the elemental images were noticeably enhanced with the radiality map, which in combination with the radiality map of the corresponding 3D PSF, resulted in the substantially improved 3D volumetric reconstruction of the cell (**Fig. 2(c,d)**). In particular, as observed, *rad*-FLFM displayed the 3D distribution of actins adhesive to the coverslip within a thin layer of ~500 nm below the axial Rayleigh range (600-800 nm for the 100×, 1.45NA objective lens), which were poorly resolvable using conventional FLFM (**Fig. 2(e,f)**). In contrast to diffraction-limited (200-300 nm in x and y) wide-field microscopy, *rad*-FLFM exhibited both the 3D imaging capability and clearly higher resolution in all three dimensions (**Fig. 2(f,g)**). For instance, the delicate structures of actin bundles separated as close as 158 nm can be resolved using *rad*-FLFM (**Fig. 2(h)**). The reconstructed images of actin bundles exhibited FWHM values

Biomedical Optics EXPRESS

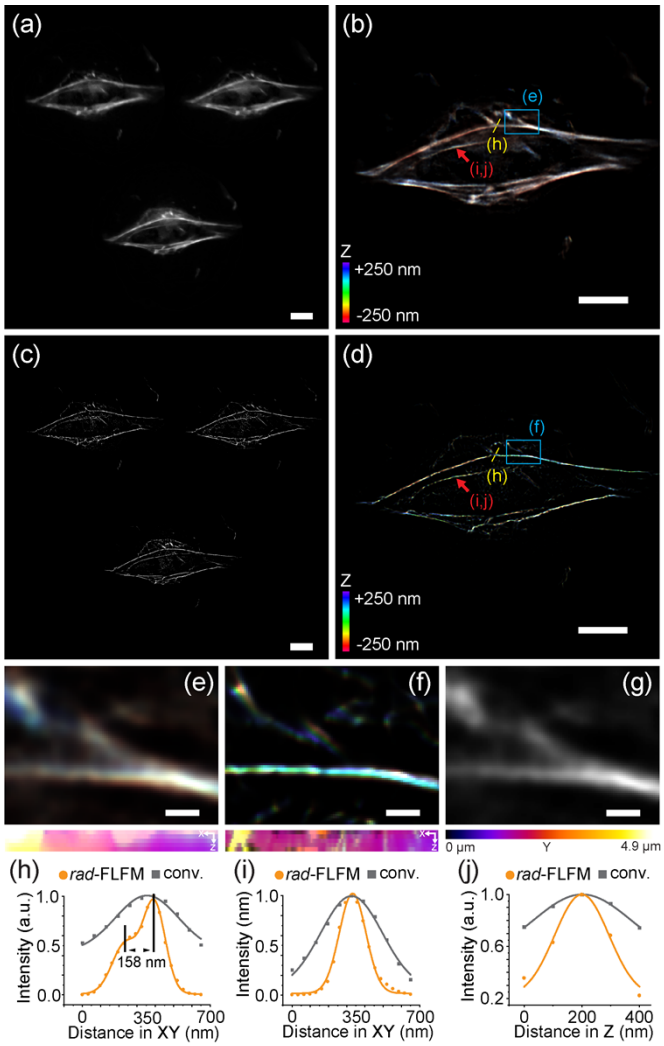

Fig. 2. Imaging actins in live HeLa cells using *rad*-FLFM. (a,b) Raw elemental light-field (a) and conventional 3D reconstructed FLFM (b) images of actins in Hela cells. (c,d) Corresponding images using *rad*-FLFM. (e,f) Zoomed-in images of the corresponding blue boxed regions in (b) and (d), respectively. The insets show the corresponding color-coded maximum intensity projection of the 3D volumes (total depth range in $Z = 500$ nm) in (e,f) along the Y axis onto the XZ plane, exhibiting the better 3D resolving ability of *rad*-FLFM from the XZ perspective. (g) Corresponding 2D wide-field image of the same region as in (e,f). (h) Cross-sectional profiles along the yellow dashed line in (b) and (d), showing resolved actin bundles separated below the diffraction limit by *rad*-FLFM. (i,j) Cross-sectional profiles of the actin bundle in both lateral and axial dimensions indicated by the red arrows in (b) and (d), showing over two-fold improvement in the FWHM values using *rad*-FLFM (172 nm and 295 nm in XY and Z, respectively) over conventional FLFM (397 nm and 623 nm in XY and Z, respectively). The depth information in (b, d, e, f) is coded as in the color-scale bar in (b, d). The Y-distance information in (e,f) insets is coded as in the corresponding Y-axis color-scale bar. Scale bars: 10 µm (a-d), 1 µm (e-g).

Biomedical Optics EXPRESS

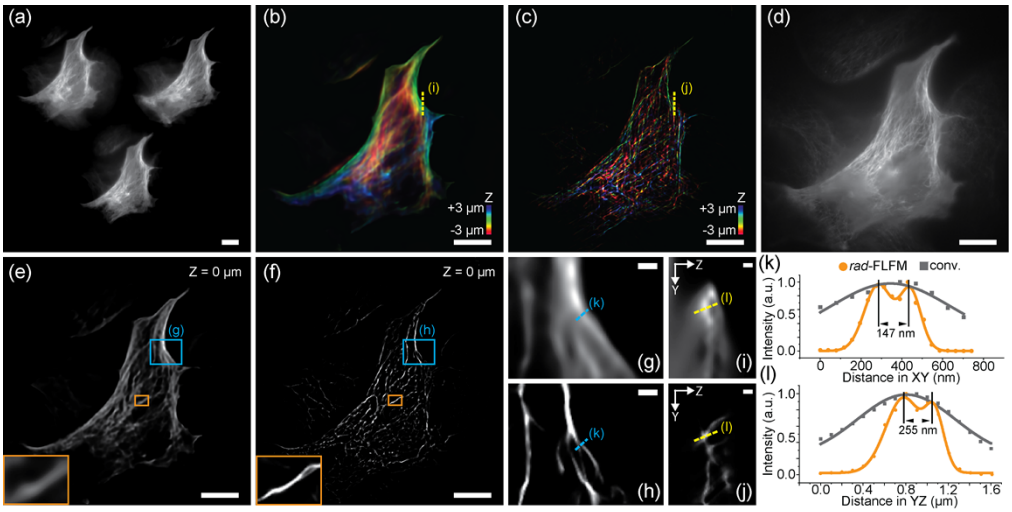

Fig. 3. Imaging microtubules in human mammary organoids using *rad*-FLFM. (a-c) Raw elemental light-field (a), conventional 3D reconstructed FLFM (b), and *rad*-FLFM (c) images of microtubules in mammary organoids. (d) Corresponding wide-field image of the same region as in (a-c). (e,f) Reconstructed focal stacks of (b,c) at $Z = 0$ μm, respectively. (g,h) Zoomed-in images of the corresponding boxed regions in (e,f), respectively. (i,j) Zoomed-in YZ views along the dashed lines in (b,c), respectively. (k,l) Cross-sectional profiles along the dashed lines in (g,h) and (i,j), respectively. The depth information in (b,c) is coded as in the corresponding color-scale bar. Scale bars: 10 μm (a-f), 1 μm (g-j).

at ~172 nm and 295 nm in the lateral and axial dimensions, respectively, showing a nearly two-fold improvement in both dimensions, as opposed to ~397 nm and 623 nm, respectively, as measured using conventional FLFM (**Fig. 2(i,j)**).

3.2. *Imaging microtubules in human mammary organoids*

Next, we conducted *rad*-FLFM imaging of microtubules labeled with Tubulin Tracker in mammary organoid (MCF10A organoid) samples derived from breast epithelial tissue using the 647-nm laser (**Fig. 3**). Consistent with conventional FLFM, the system recorded the incident light field from single cells within the organoid in elemental light-field images (**Fig. 3(a)**), recovering a volume of 67 μm × 67 μm × 6 μm at a volume acquisition time of 0.2 s. In contrast, *rad*-FLFM exhibited a substantially enhanced resolution in all three dimensions throughout the volume compared to that of conventional FLFM (**Fig. 3(b,c)**). Notably, in addition to the resolution enhancement, the volumetric ability of *rad*-FLFM allows capturing densely packed microtubules across a 6× extended depth of focus (DOF, ~6 μm) that were otherwise out-of-focus and less observable using wide-field microscopy (**Fig. 3(c,d)**). For conventional FLFM, the DOF can be derived as the full width of the axial PSF of the elemental images (i.e., 2× the FWHM value in the axial direction), considering the fact that the deconvolution in the reconstruction process is able to retrieve the diffracted information outside of the Rayleigh range of the axial PSF [30]. Using this model, the DOF can be obtained at 4.41 μm for the dark red emission. For *rad*-FLFM, we reason that the radiality analysis effectively enhances and thus retrieves the formerly defocused axial range beyond the Rayleigh range, thereby offering a moderate improvement of the DOF. Furthermore, the synthesized focal stacks of *rad*-FLFM exhibited finer structural details over conventional FLFM (**Fig. 3(e,f)**). This improvement, for instance, leads to clearly resolved microtubule filaments separated by 147 nm in the lateral dimension and 255 nm in the axial

Biomedical Optics EXPRESS

dimension using the *rad*-FLFM system, presenting a two-fold enhancement in spatial resolution over the diffraction limit in all three dimensions (**Fig. 3(g-l)**).

3.3. Imaging peroxisomes in live COS-7 cells

Lastly, we imaged GFP-labeled peroxisomes in live COS-7 cells using *rad*-FLFM (**Fig. 4**). Peroxisomes are intracellular organelles that exhibit distinct small-scale and highly-dynamic spatiotemporal features in the cytoplasm, posing a challenge for conventional wide-field or

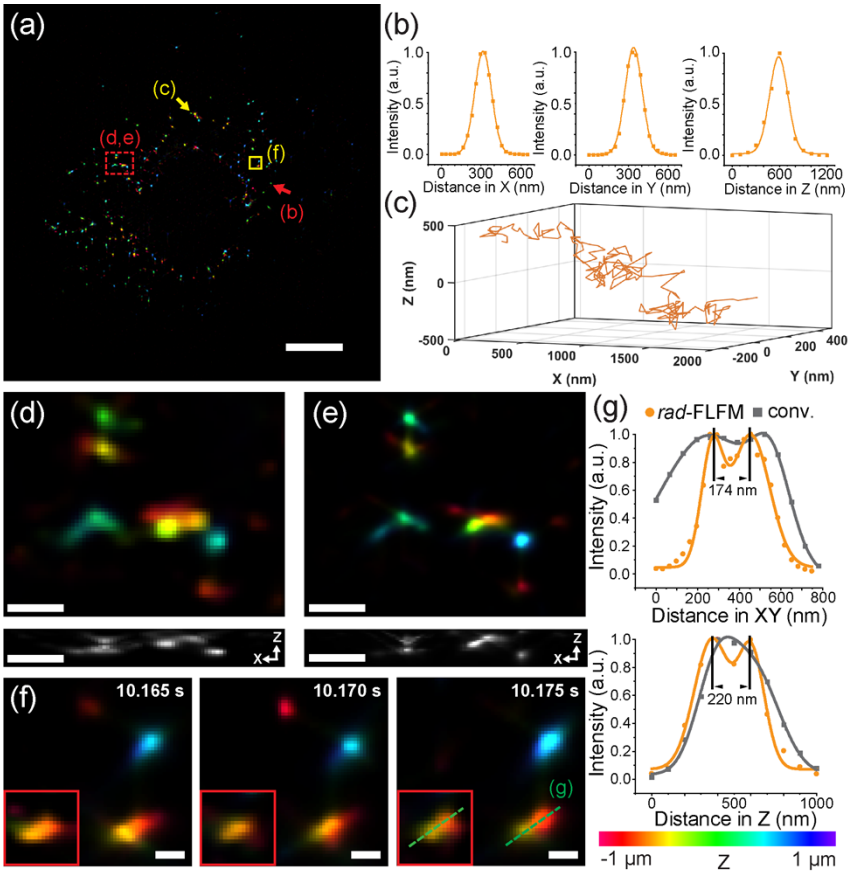

Fig. 4. Imaging peroxisomes in live COS-7 cells using *rad*-FLFM. (a) 3D reconstructed *rad*-FLFM image of peroxisomes in live COS-7 cells taken at a volume acquisition time of 5 ms. (b) Cross-sectional profiles of an individual peroxisome marked by the red arrow in (a), exhibiting FWHM values of 151 nm, 152 nm, and 273 nm in X, Y, and Z, respectively. (c) 3D tracking of the peroxisome marked by the yellow arrow in (a) over a time course of 1 second. (d,e) Zoomed-in images of the corresponding red dashed boxed region in (a) for conventional FLFM (d) and *rad*-FLFM (e). The insets show the corresponding maximum intensity projection of the volumes of (d,e) onto the XZ plane (total depth range in $Z = 2$ μm). (f) Zoomed-in images of the yellow solid boxed region in (a) at continuous time points $t = 10.165$ s, 10.170 s and 10.175 s. The insets show the corresponding images of the two nearby peroxisomes taken with conventional FLFM. (g) Cross-sectional profiles across the centers of the two peroxisomes indicated by the dashed line in (f), showing their resolvable separation of 174 nm and 220 nm in the lateral and axial dimensions, respectively, using *rad*-FLFM. Scale bars: 10 μm (a), 1 μm (d,e), 300 nm (f).

Biomedical Optics EXPRESS

scanning-based microscopy to capture their collective behaviors within a significant cellular volume. Here, *rad*-FLFM realized time-lapse, volumetric observation of peroxisomes at a volume acquisition time of 5 ms over thousands of time points without noticeable photodamage (**Fig. 4(a)**). In particular, the reconstructed 3D images of individual peroxisomes exhibited FWHM values of ∼150 nm and ∼ 300 nm in the lateral and axial dimensions, respectively, consistent with both the known diameter of peroxisomes as low as 0.1 μm [43] and the expected sub-diffraction-limited resolution of the *rad*-FLFM system (**Fig. 4(b)**). The spatiotemporal resolution and volumetric ability of *rad*-FLFM allow for the continuous acquisition of the fast-moving positions of each peroxisome in the 3D cellular space, and by localizing the reconstructed images, their trajectories can be individually formulated with a nanometer-level precision (**Fig. 4(c)**). In comparison with conventional FLFM, *rad*-FLFM demonstrated an enhanced observation of peroxisomes in all three dimensions, allowing us to visualize interacting entities as close as 150-200 nm and 200-300 nm in the lateral and axial dimensions, respectively, offering a ∼2× improvement in the 3D resolution over that of conventional FLFM at 300-500 nm [30] (**Fig. 4(d-g)**). These results verified the ability of *rad*-FLFM to capture 3D subcellular structural and dynamic details, promising a particularly compelling solution to live-cell imaging and biological discoveries.

4. Conclusions

In summary, we have demonstrated *rad*-FLFM, a 3D live-cell super-resolution imaging method based on image denoising, radiality analysis, and light-field imaging. Compared with wide-field microscopy, *rad*-FLFM offers volumetric, snapshot imaging of single-cell specimens with two-fold improvement in 3D resolution beyond the diffraction limit, milliseconds temporal resolution, and six-fold extension of the imaging depth. The system retains the advantages of light-field imaging techniques such as simple instrumentation, low photodamage for live-cell observation, and high compatibility with various cell protocols. We anticipate *rad*-FLFM to offer a promising 3D super-resolution paradigm for interrogating intracellular structural and functional complexities in a broad range of cell biological research.

Appendices

Appendix 1. Algorithmic settings for rad-FLFM

For all three types of biological sample (i.e., HeLa cell, MCF10A organoid, and COS-7 cell), the SRRF setting for the radiality analysis and corresponding iteration times for the Richardson-Lucy deconvolution are listed below:

Table 1. Settings for Radiality Analysis and Reconstruction

Table	HeLa cell	MCF10A organoid	COS-7 cell
Ring Radius	0.5		
Radiality Magnifications	8		
Axes in Ring	8		
Iteration times	3	5	5

Do Gradient Smoothing, *Do Intensity Weighting*, and *Minimize SRRF patterning* are contained in the Advanced Settings section of the SRRF ImageJ Plugin as checkbox terms.

Funding. National Science Foundation (DBI2145235, EFMA1830941); National Institutes of Health (R01GM123517, R35GM124846).

Acknowledgements. We acknowledge the support of the faculty start-up fund of Georgia Institute of Technology (to S.J.), Marvin H. and Nita S. Floyd Research Fund (to S.J.), and Price Gilbert Jr Chair Fund (to S.T.).

Disclosures. The authors declare that there are no conflicts of interest to this article.

Biomedical Optics EXPRESS

Data Availability. The codes for ACsN and Richardson-Lucy deconvolution for Fourier Light-field microscopy has been written in MATLAB (MathWorks), and their latest versions are available through Ref. [44] and Ref. [45], respectively. Radiality analysis is performed using SRRF ImageJ and is available in Ref. [46]. The rolling-ball algorithm is provided as a default function in ImageJ.

References

1. Y. M. Sigal, R. Zhou, and X. Zhuang, "Visualizing and discovering cellular structures with super-resolution microscopy," Science **361**(6405), 880–887 (2018).
2. S. Skylaki, O. Hilsenbeck, and T. Schroeder, "Challenges in long-term imaging and quantification of single-cell dynamics," Nat. Biotechnol. **34**(11), 1137–1144 (2016).
3. E. A. Specht, E. Braselmann, and A. E. Palmer, "A Critical and Comparative Review of Fluorescent Tools for Live-Cell Imaging," Annu. Rev. Physiol. **79**(1), 93–117 (2017).
4. G.-C. Yuan, L. Cai, M. Elowitz, T. Enver, G. Fan, G. Guo, R. Irizarry, P. Kharchenko, J. Kim, S. Orkin, J. Quackenbush, A. Saadatpour, T. Schroeder, R. Shivdasani, and I. Tirosh, "Challenges and emerging directions in single-cell analysis," Genome Biol. **18**(1), 84 (2017).
5. P. P. Laissue, R. A. Alghamdi, P. Tomancak, E. G. Reynaud, and H. Shroff, "Assessing phototoxicity in live fluorescence imaging," Nat. Methods **14**(7), 657–661 (2017).
6. W. C. Lemon and K. McDole, "Live-cell imaging in the era of too many microscopes," Curr. Opin. Cell Biol. **66**, 34–42 (2020).
7. N. Scherf and J. Huisken, "The smart and gentle microscope," Nat. Biotechnol. **33**(8), 815–818 (2015).
8. S. W. Hell, "Far-Field Optical Nanoscopy," Science **316**(5828), 1153–1158 (2007).
9. B. Huang, H. Babcock, and X. Zhuang, "Breaking the diffraction barrier: Super-resolution imaging of cells," Cell **143**(7), 1047–1058 (2010).
10. Z. Liu, L. D. Lavis, and E. Betzig, "Imaging live-cell dynamics and structure at the single-molecule level," Mol. Cell **58**(4), 644–659 (2015).
11. T. Dertinger, R. Colyer, G. Iyer, S. Weiss, and J. Enderlein, "Fast, background-free, 3D super-resolution optical fluctuation imaging (SOFI)," Proc. Natl. Acad. Sci. U. S. A. **106**(52), 22287–22292 (2009).
12. N. Gustafsson, S. Culley, G. Ashdown, D. M. Owen, P. M. Pereira, and R. Henriques, "Fast live-cell conventional fluorophore nanoscopy with ImageJ through super-resolution radial fluctuations," Nat. Commun. **7**(1), 12471 (2016).
13. R. F. Laine, H. S. Heil, S. Coelho, J. Nixon-Abell, A. Jimenez, T. Galgani, A. Stubb, G. Follain, S. Culley, G. Jacquemet, B. Hajj, C. Leterrier, and R. Henriques, *High-fidelity 3D live-cell nanoscopy through data-driven enhanced super-resolution radial fluctuation*, (Cold Spring Harbor Laboratory, 2022).
14. S. Culley, K. L. Tosheva, P. M. Pereira, and R. Henriques, "SRRF: Universal live-cell super-resolution microscopy," Int. J. Biochem. Cell Biol. **101**, 74–79 (2018).
15. R. Ehrlich, V. Wulf, A. Hendler-Neumark, B. Kagan, and G. Bisker, "Super-Resolution Radial Fluctuations (SRRF) nanoscopy in the near infrared," Opt. Express **30**(2), 1130–1142 (2022).
16. H. Q. Ma, F. Long, S. Q. Zeng, and Z. L. Huang, "Fast and precise algorithm based on maximum radial symmetry for single molecule localization," Opt. Lett. **37**(13), 2481–2483 (2012).
17. R. Parthasarathy, "Rapid, accurate particle tracking by calculation of radial symmetry centers," Nat. Methods **9**(7), 724–726 (2012).
18. M. Broxton, L. Grosenick, S. Yang, N. Cohen, A. Andalman, K. Deisseroth, and M. Levoy, "Wave optics theory and 3-D deconvolution for the light field microscope," Opt. Express **21**(21), 25418–25439 (2013).
19. M. Levoy, Z. Zhang, and I. McDowall, "Recording and controlling the 4D light field in a microscope using microlens arrays," J. Microsc. **235**(2), 144–162 (2009).
20. L. Marc, N. Ren, A. Adams, M. Footer, M. Horowitz, M. Levoy, R. Ng, A. Adams, M. Footer, and M. Horowitz, "Light field microscopy," ACM Trans. Graph. **25**(3), 924–934 (2006).
21. R. Prevedel, Y. G. Yoon, M. Hoffmann, N. Pak, G. Wetzstein, S. Kato, T. Schrodel, R. Raskar, M. Zimmer, E. S. Boyden, and A. Vaziri, "Simultaneous whole-animal 3D imaging of neuronal activity using light-field microscopy," Nat. Methods **11**(7), 727–730 (2014).
22. A. Llavador, J. Sola-Pikabea, G. Saavedra, B. Javidi, and M. Martinez-Corral, "Resolution improvements in integral microscopy with Fourier plane recording," Opt. Express **24**(18), 20792–20798 (2016).
23. L. Cong, Z. Wang, Y. Chai, W. Hang, C. Shang, W. Yang, L. Bai, J. Du, K. Wang, and Q. Wen, "Rapid whole brain imaging of neural activity in freely behaving larval zebrafish (Danio rerio)," eLife **6**, e28158 (2017).
24. G. Scrofani, J. Sola-Pikabea, A. Llavador, E. Sanchez-Ortiga, J. C. Barreiro, G. Saavedra, J. Garcia-Sucerquia, and M. Martinez-Corral, "FIMic: design for ultimate 3D-integral microscopy of in-vivo biological samples," Biomed. Opt. Express **9**(1), 335–346 (2018).
25. C. Guo, W. Liu, X. Hua, H. Li, and S. Jia, "Fourier light-field microscopy," Opt. Express **27**(18), 25573–25594 (2019).
26. K. Yanny, N. Antipa, W. Liberti, S. Dehaeck, K. Monakhova, F. L. Liu, K. Shen, R. Ng, and L. Waller, "Miniscope3D: optimized single-shot miniature 3D fluorescence microscopy," Light: Sci. Appl. **9**(1), 171 (2020).
27. Y. Xue, I. G. Davison, D. A. Boas, and L. Tian, "Single-shot 3D wide-field fluorescence imaging with a Computational Miniature Mesoscope," Sci. Adv. **6**(43), eabb7508 (2020).

Biomedical Optics EXPRESS

28. W. Liu, G.-A. R. Kim, S. Takayama, and S. Jia, "Fourier light-field imaging of human organoids with a hybrid point-spread function," Biosens. Bioelectron. **208**, 114201 (2022).
29. Z. Zhang, L. Bai, L. Cong, P. Yu, T. Zhang, W. Shi, F. Li, J. Du, and K. Wang, "Imaging volumetric dynamics at high speed in mouse and zebrafish brain with confocal light field microscopy," Nat. Biotechnol. **39**(1), 74–83 (2021).
30. X. Hua, W. Liu, and S. Jia, "High-resolution Fourier light-field microscopy for volumetric multi-color live-cell imaging," Optica **8**(5), 614–620 (2021).
31. R. R. Sims, S. A. Rehman, M. O. Lenz, S. I. Benaissa, E. Bruggeman, A. Clark, E. W. Sanders, A. Ponjavic, L. Muresan, S. F. Lee, and K. O'Holleran, "Single molecule light field microscopy," Optica **7**(9), 1065–1072 (2020).
32. S. Liu, M. J. Mlodzianoski, Z. Hu, Y. Ren, K. McElmurry, D. M. Suter, and F. Huang, "sCMOS noise-correction algorithm for microscopy images," Nat. Methods **14**(8), 760–761 (2017).
33. B. Mandracchia, X. Hua, C. Guo, J. Son, T. Urner, and S. Jia, "Fast and accurate sCMOS noise correction for fluorescence microscopy," Nat. Commun. **11**(1), 94 (2020).
34. P. Coupe, M. Munz, J. V. Manjon, E. S. Ruthazer, and D. L. Collins, "A CANDLE for a deeper in vivo insight," Med. Image Anal. **16**(4), 849–864 (2012).
35. J. He, Y. Cai, J. Wu, and Q. Dai, "Spatial-temporal low-rank prior for low-light volumetric fluorescence imaging," Opt. Express **29**(25), 40721–40733 (2021).
36. S. R. Sternberg, "Biomedical Image-Processing," Computer **16**(1), 22–34 (1983).
37. M. Laasmaa, M. Vendelin, and P. Peterson, "Application of regularized Richardson-Lucy algorithm for deconvolution of confocal microscopy images," J. Microsc. **243**(2), 124–140 (2011).
38. L. B. Lucy, "An iterative technique for the rectification of observed distributions," The Astronomical Journal **79**, 745 (1974).
39. W. H. Richardson, "Bayesian-based iterative method of image restoration," J. Opt. Soc. Am. **62**(1), 55 (1972).
40. S. Lee, J. Chang, S. M. Kang, E. Parigoris, J. H. Lee, Y. S. Huh, and S. Takayama, "High-throughput formation and image-based analysis of basal-in mammary organoids in 384-well plates," Sci. Rep. **12**(1), 317 (2022).
41. E. Parigoris, S. Lee, D. Mertz, M. Turner, A. Y. Liu, J. Sentosa, S. Djomehri, H. C. Chang, K. Luker, G. Luker, C. G. Kleer, and S. Takayama, "Cancer cell invasion of mammary organoids with basal-in phenotype," Adv. Healthcare Mater. **10**(4), 2000810 (2021).
42. Y. C. Tung, A. Y. Hsiao, S. G. Allen, Y. S. Torisawa, M. Ho, and S. Takayama, "High-throughput 3D spheroid culture and drug testing using a 384 hanging drop array," Analyst **136**(3), 473–478 (2011).
43. J. J. Smith and J. D. Aitchison, "Peroxisomes take shape," Nat. Rev. Mol. Cell Biol. **14**(12), 803–817 (2013).
44. Jia Lab, "Automatic correction for sCMOS-related noise," Github, 2022, https://github.com/ShuJiaLab/ACsN
45. Jia Lab, "High-resolution Fourier light-field microscopy for volumetric multi-color live-cell imaging," Github, 2022, https://github.com/ShuJiaLab/HR-FLFM
46. Henriques Lab, "Super-resolution radial fluctuations (SRRF)," Github, 2022, https://github.com/HenriquesLab/NanoJ-SRRF